A selective ion replacement strategy for the synthesis of copper doped carbon nitride nanotubes with improved photocatalytic hydrogen evolution

Xiaoxiao Yan[a], Zhiyuan Jia[a], Haibing Che[a], Shuqun Chen[a], Peng Hu[a,*], Jinshu Wang[a,*], Lianzhou Wang[a,b,*]

[a] School of Materials Science and Engineering, Beijing University of Technology, Beijing, 100124, PR China
[b] School of Chemical Engineering and Australian Institute for Bioengineering and Nanotechnology, The University of Queensland, Brisbane, QLD, 4072, Australia

A B S T R A C T

Developing new strategy to efficiently improve the photocatalytic activity of graphitic carbon nitride (g-C_3N_4) for hydrogen evolution is critical for its application in solar energy utilization. In this work, an innovative selective cation replacement process is developed to synthesize copper doped g-C_3N_4 nanotubes driven by the ion–dipole interaction of metal ions in g-C_3N_4. The tri-s-triazine units may act as stable frameworks in the sequential cation exchange reaction process, which subsequently leads to the formation of Cu doped g-C_3N_4 with high specific surface area and nanotube structures. The obtained g-C_3N_4 exhibits greatly enhanced visible-light-driven hydrogen evolution of 3.02 mmol h^{-1} g^{-1}, which is about 13 times higher than that of pristine one. Detailed characterization reveals the underlying mechanism of the improved photocatalytic performance on the newly developed g-C_3N_4, which can provide valuable guides to rationally design new efficient photocatalysts.

1. Introduction

Engineering semiconductors for photocatalytic water splitting is important for efficient conversion of solar energy to chemical fuels. For this purpose, a large number of semiconductors, including oxides, nitrides, sulfides and their composite etc., have been investigated and developed as potential candidates for photocatalytic H_2/O_2 evolution or overall water splitting [1–8]. In particular, graphitic carbon nitride (g-C_3N_4), a graphite-like layered material with bandgap of about 2.7 eV, has been exemplified as a low-cost metal-free polymeric photocatalyst for solar energy conversion due to its suitable band positions, attractive electronic properties and high stability [9]. Inspired by the first report on visible-light driven photocatalytic water splitting of g-C_3N_4 [10], promising progresses have been achieved in g-C_3N_4-based photocatalysis [11,12]. In spite of this, pure g-C_3N_4 still suffers from unsatisfactory quantum efficiency for solar hydrogen evolution because of its low specific surface area (normally reported is about 12–15 m^2 g^{-1}), insufficient solar light absorption (less than 450 nm) and fast recombination of photoexcited carriers originating from its organic π-conjugated molecules structure [13]. All these issues hinder g-C_3N_4 to be an effective photocatalyst for efficient solar-light driven water splitting.

Inspired by the modification of inorganic semiconductors for photocatalysis applications, a series of strategies, such as morphology control [14,15], heterostructure construction [16,17], elemental doping [18,19] and copolymerization [20,21], have been exploited to improve the photocatalytic performance of carbon nitride. Significantly, elemental doping has been considered as one of the most efficient approaches to adjust the electronic structure of g-C_3N_4, making it possible to broaden the light absorption range and suppress the recombination of photoexcited carriers [22,23]. Various dopants, including alkali metals [24,25], transition metals [26–28] and non-metal elements [29,30] etc., have been employed to enhance the photocatalytic performance. Generally, elemental doping is realized accompanied by the in situ thermal polycondensation process for g-C_3N_4 synthesis, and uncontrolled structures with small surface areas are usually obtained due to the high synthesis temperature. For example, directly heating the mixture of melamine and copper chloride leads to formation of bulk Cu doped g-C_3N_4 (Cu-g-C_3N_4) with irregular particle shape [27]. This limits the possibility for further improving the photocatalytic properties due to the insufficient surface active sites for catalysis reaction. Although nanostructural design of g-C_3N_4, such as porous structure, is an efficient way to provide large surface area and channels for mass diffusion and charge migration. The use of hard templates suffers the drawbacks of complexity, i.e., costly synthesis process and low yield [15,31], therefore, synthesis of doped g-C_3N_4 with well-controlled nanostructures by a simple and facile route is highly desired.

* Corresponding authors at: School of Materials Science and Engineering, Beijing University of Technology, Beijing, 100124, PR China.
E-mail addresses: pengh@bjut.edu.cn (P. Hu), wangjsh@bjut.edu.cn (J. Wang), l.wang@uq.edu.au (L. Wang).
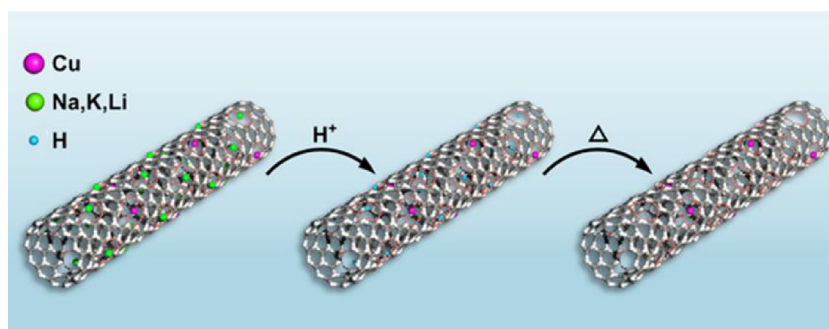
Fig. 1. Schematic illustration of selective cation replacement strategy for the synthesis of copper doped carbon nitride, the porous nanotuebs could be well preserved during sequential cations replacement process.

Cation exchange reaction is a feature reaction in inorganic ionic nanocrystals in which the original cations could be replaced by guest cations with lower solubility, while the crystallographic characteristic could be well preserved due to the unchanged anions framework [32]. This reaction leads to the composition tuning of the obtained nanocrystals. In this work, an innovative sequential cations replacement process is firstly developed to synthesize Cu-g-C_3N_4 with well-controlled nanostructure. The mixture of eutectic salts is used as template in thermal polycondensation process for the synthesis of Cu-g-C_3N_4, which could be selectively removed by an easier way compared to the adoption of hard template, leading to the formation of mesoporous nanotubes with high yield (see the Schematic illustration in Fig. 1). The newly obtained products exhibit higher specific surface areas, improved visible light absorbance and well suppressed recombination of carriers compared to pristine g-C_3N_4, subsequently, ～13 times improvement on photocatalytic properties for water splitting.

2. Materials and methods

2.1. Materials

All the chemicals are analytical grade and used as received without further purification.

2.2. Synthesis of copper doped mesoporous g-C3N4 nanotubes

Alkali metals and copper ions were first co-doped into g-C_3N_4 via in situ thermal polycondensation process for g-C_3N_4 synthesis by a modified eutectic molten salt method [33]. For a typical synthesis process, the mixture of eutectic salts (LiCl-NaCl-KCl, 1:1:1 wt ratio) and melamine with weight ratio of 10:1 was firstly dissolved into distilled water, then different amount of $CuCl_2 \cdot 2H_2O$ was added as doping agent. The mixture solution was dried by rotary evaporation at 80 °C. After that, the precursors were finely ground in a mortar and transferred to a quartz crucible with cover. The powder was heated to 500 °C for 2 h at a heating rate of 5 °C/min., and then raised to 520 °C for another 2 h. The resulting yellow powder was washed three times with deionized water and absolute ethanol, respectively. Finally, it was collected by centrifugation and dried at 60 °C in vacuum oven overnight to form multi-cation co-doped mesoporous g-C_3N_4 nanotubes.

Selective ion exchange reaction was conducted by dispersing the obtained products into 1 M HCl aqueous solutions at room temperature for 3 h. This sample was collected by centrifuging and washed with deionized water and absolute ethanol to remove residual acid, which leads to the generation of protonated g-C_3N_4 nanotubes with Cu doping. Finally, the introduced protons could be removed by heating the sample at 400 °C for 2 h (Cu-g-C_3N_4 nanotubes). The pure mesoporous g-C_3N_4 nanotubes (g-C_3N_4 nanotubes) were synthesized by same process without adding $CuCl_2 \cdot 2H_2O$.

2.3. Synthesis of bulk g-C3N4 and Cu doped bulk g-C3N4

The bulk g-C_3N_4 was synthesized by directly thermal polycondensation process using melamine as single precursor, the heat treatment parameters were same as above without post-treatment. Bulk Cu doped g-C_3N_4 (Cu-g-C_3N_4) was synthesized by using the mixture of melamine and copper chloride as precursors follows the same thermal polycondensation process.

2.4. Characterizations

The crystal phases of obtained products were firstly studied by X-ray powder diffraction (XRD) on a SHIMADZU XRD-7000 XRD diffractometer using Cu Kα radiation. Scanning electron microscopy (SEM) and Energy Dispersive X-ray spectroscopic (EDS) analysis were conducted on a Hitachi S-4800N scanning electron microscopy equipped with energy-dispersive X-ray analysis system. Transmission electron microscopy (TEM, JEM-2010) was used to observe the detailed morphology and elemental distribution of the products. The Brunauer-Emmett-Teller (BET) surface area was performed on Micromerities ASAP 2020 with porosity analyzer. The proton amount in obtained products was determined by Vario EL III Elementar. UV–vis absorption spectra were recorded on a UV-2450 Ultraviolet-visible spectrophotometer (Shimadzu). The organic groups of the samples were performed by FT-IR spectra on a PerkinElmer spectrometer. X-ray photoelectron spectra (XPS) was measured on a PHI 5300 ESCA system with a 150 W monochromated Al Kα line source. The solid-state ^{13}C Nuclear Magnetic Resonance (NMR) spectra were performed on a Bruker 400 MHz WB Solid-State NMR Spectrometer. Photoluminescence (PL) spectra were measured using a JASCO-FP6200 at room temperature. Time-resolved photoluminescence (PL) spectroscopy was conducted using FLsp920 Fluorescence spectrometer (Edinburgh Instruments), and using a Xe lamp as excitation source at 397 nm.

2.5. Photocatalytic testing

Photocatalytic hydrogen evolution was carried out in a gas closed circulation system with a Pyrex top-irradiation reaction vessel. A 300 W Xe lamp was used as light source with a cutoff filter (λ > 420 nm) to remove the UV part of the light. The catalyst (0.05 g) was dispersed in 100 ml of aqueous solution containing 10 vol% triethanolamine as sacrificial reagent, and 3 wt.% Pt co-catalyst was photodeposited on the as synthesized catalyst in situ using $H_2PtCl_6 \cdot 6H_2O$ as a precursor. Before light irradiation, the system was sealed up and purged with nitrogen gas to remove residual air. Evolved hydrogen was detected by a gas chromatograph with a thermal conductivity detector.

2.6. Photoelectrochemical measurements

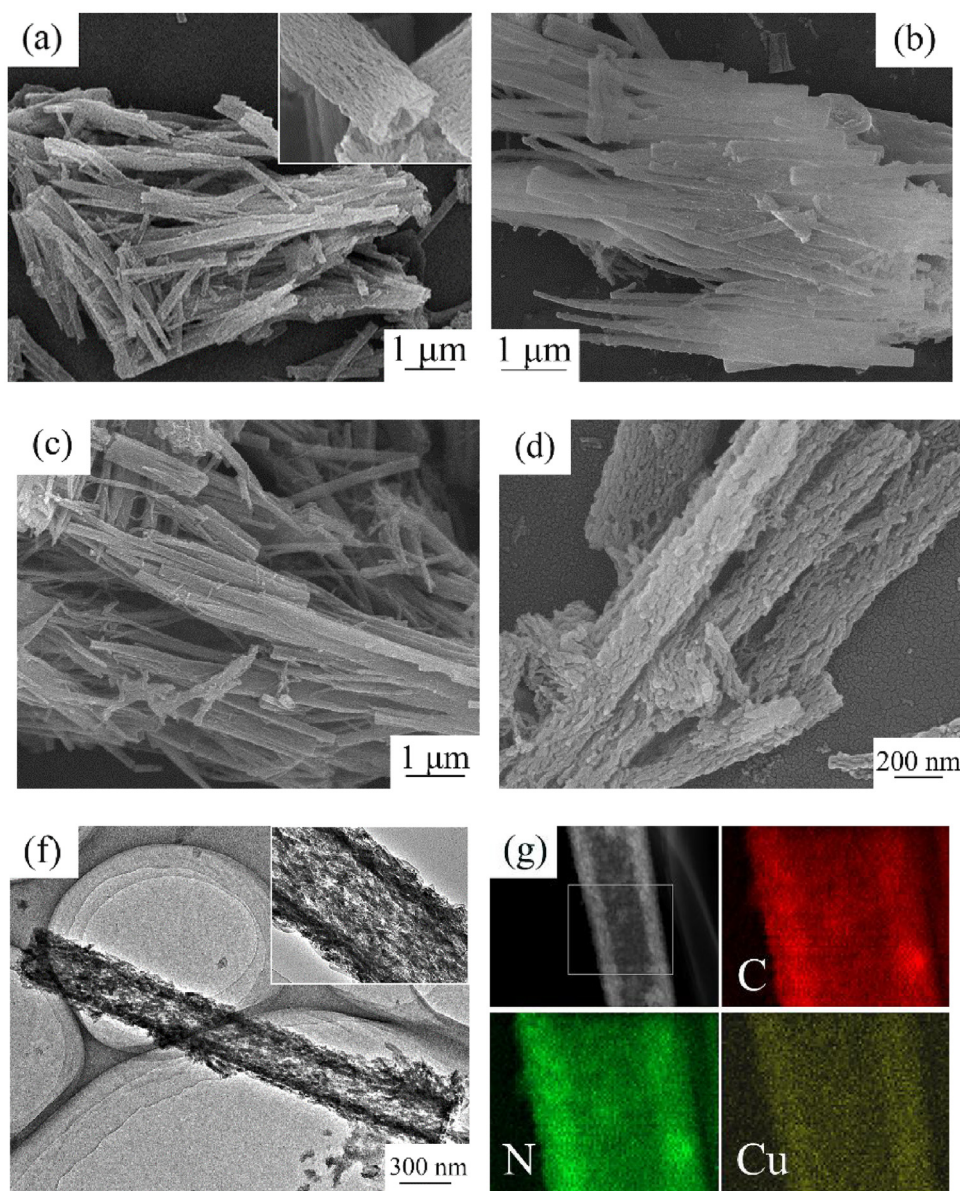Photocurrent measurements were carried out in a three-electrode

Fig. 2. SEM images of (a) multi-cation doped g-C$_3$N$_4$, (b) protonated Cu-g-C$_3$N$_4$ (c) and (d) Cu-g-C$_3$N$_4$, (f) TEM image and (g) elemental mapping of obtained Cu-g-C$_3$N$_4$.

configuration in an aqueous Na$_2$SO$_4$ electrolyte (0.1 M) by an electro-chemical analyzer (CHI-660B, Shanghai Chenhua, China). As prepared sample, platinum wire and saturated calomel electrode (SCE) were used as working electrode, counter electrode and reference electrode, re-spectively. A 300 W xenon lamp with a 420 nm cut-off filter was used as light source. Electrochemical impedance spectra (EIS) was performed via a three-electrode cell by applying 5 mV amplitude over the fre-quency range was from 0.1 to 100,000 Hz.

3. Results and discussion

Morphology evolution during sequential ion replacement process were firstly analyzed by field-emission scanning electron microscopy (SEM) and transmission electron microscopy (TEM) as shown in Fig. 2. From Fig. 2a–d, the typical morphology of products obtained at dif-ferent stages can be observed. Multi-cations doped g-C$_3$N$_4$ synthesized by in situ thermal polycondensation process exhibits tubular appear-ance with length and width about 2–5 μm and 300 nm (Fig. 2a), re-spectively, and the formation mechanism could be attributed to the self-

template function of eutectic molten salts flux (NaCl-KCl-LiCl)[18,33]. Magnified SEM image doped in Fig. 2a presents the mesoporous structure of the obtained products, and the walls of the nanotubes are composed of elongated nanoparticles. It worth mentioning that the mesoporous tubular structure could be well preserved during protona-tion process (Fig. 2b), which is totally different from the broken texture of protonation of bulk g-C$_3$N$_4$ [34]. This will facilitate the morphology control of Cu-g-C$_3$N$_4$ mesoporous nanotubes by further dehydrogena-tion process presented in Fig. 2c and d. The structure characteristics of the final products was further revealed by TEM observation in Fig. 2e, and the bright contrast of the particle confirms the existence of hollow structures in the resulting products, well consistent with the SEM ob-servation. The elemental mapping exhibits a uniform distribution of C, N and Cu in obtained nanotubes (Fig. 2f), confirming the successful doping of Cu within g-C$_3$N$_4$. Nitrogen adsorption–desorption analysis in Fig. 3 presents the typical feature of porous structure (closed to types IV with H3 hysteresis loop), which could be attributed to the existence of slit pores formed by the packing of elongated nanoparticles, as con-firmed by SEM and TEM observation. The calculated specific surface
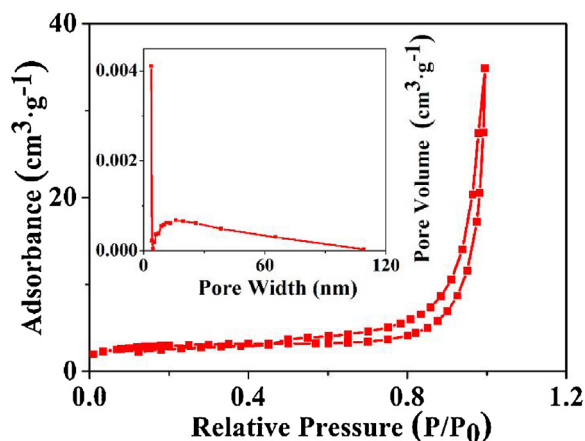
Fig. 3. N_2 adsorption-desorption isotherms of as-synthesized photocatalyst. Inset: Pore size distribution of the sample.

area and average pore size were about 116 m^2 g^{-1} and 13.36 nm, respectively.

EDS analysis reveals the compositional change during the reaction process (Fig. S1). At the first stage of thermal polycondensation process, the obtained products were composed of Na, K, Cu, C, N and Cl (Li is undetectable by EDS). After protonation, the alkali ions were completely removed with preservation of Cu. The hydrogen content was determined to be 1.62 wt. % by detailed elemental analysis. Further heat treatment could remove the introduced proton and result in the formation of Cu-g-C$_3$N$_4$. The composition of final products is further confirmed by XPS analysis (Fig. S2).

The structural information during sequential reaction stages was further investigated by XRD analysis. From the XRD pattern in Fig. 4a, it is seen that bulk g-C$_3$N$_4$ shows two characteristic peaks at 13° and 27°, which can be assigned to the (100) and (002) crystal planes of g-

C$_3$N$_4$, representing in-plane packing and interfacial aromatic stacking [35], respectively. While for the metal doped g-C$_3$N$_4$, all the samples display broad diffraction peaks with reduced intensity due to the inhibition of polymerization by dopants and small crystal size of obtained nanotubes[36,37]. In addition, the diffraction peaks of (002) shift to a lower angle after Cu doping, indicating the increased interplanar distance by elemental doping[14,26].

The structure of the intermediate products was further analyzed by ^{13}C MAS NMR spectroscopy (Fig. 4b). The samples obtained at different reaction steps show similar spectra compared to bulk g-C$_3$N$_4$. Two resolved resonances at $\delta_1 = 156$ and $\delta_1 = 164.4$ ppm could be observed and assigned to C(i) atoms of CN$_3$ group and C(e) atoms in CN$_2$(NH$_x$)) [38,39], respectively, illustrating the formation of C$_3$N$_4$ frameworks in as synthesized products (which could be further confirmed by FT-IR spectra shown in Fig. 4c). In addition, the peak of metal doped C$_3$N$_4$ slightly shifts to about 163.3 ppm and 156.5 ppm, respectively, indicating the interaction between metal ions and the carbon C$_3$N$_4$ plane [40].

Fig. 4d presents the UV–vis diffuse reflectance spectra of different g-C$_3$N$_4$. Although all of the products displayed light absorption in the visible range, the ions doped g-C$_3$N$_4$ all revealed higher absorption shoulder with red-shift absorption edge compared to that of bulk g-C$_3$N$_4$, indicating their improved ability for light harvesting. The change of absorption spectra could be well explained by the band structures of obtained products. According to a previous report [41], the valance band of g-C$_3$N$_4$ is mainly composed of N2p orbitals, while both C2p and N2p orbitals contribute to the conduction band. Introducing alkali and Cu ions could all cause the positive shift of valance band due to the donated electrons by K and Na atoms and electrical structure change by Cu atoms to g-C$_3$N$_4$, respectively [42,23], resulting in decreased band gap. However, the enlarged band gap could be observed for protonated g-C$_3$N$_4$ [34], which may originate from elevated conduction band by the contribution of H 1 s orbital with higher energy level [43]. As indicated, the alkali metal and Cu ions co-doped g-C$_3$N$_4$ exhibit the
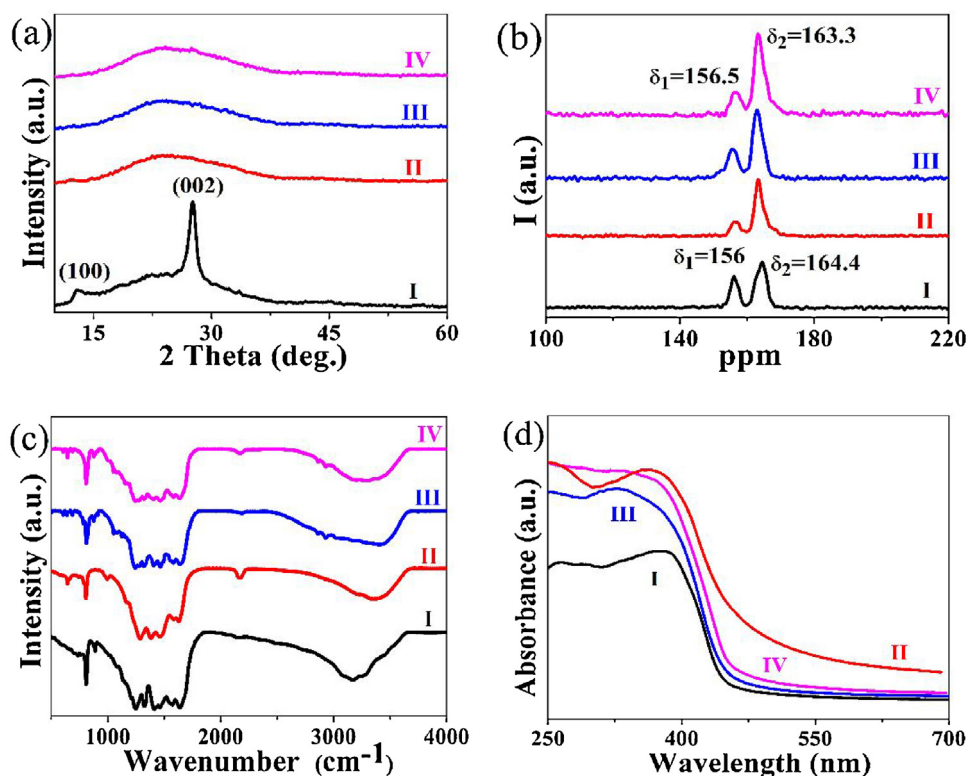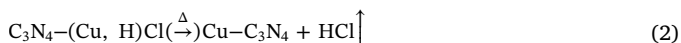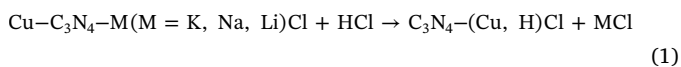

Fig. 4. (a) XRD, (b) NMR, (c) FT-IR and (d) UV–vis spectra of products obtained at different reaction stages. The curves I, II, III and IV in (a)–(d) represent the bulk g-C$_3$N$_4$, metal ions doped g-C$_3$N$_4$, protonated Cu-g-C$_3$N$_4$ and Cu-g-C$_3$N$_4$ respectively.

strongest ability for light absorption, and then gradually decreased for Cu-g-C_3N_4 nanotubes and protonated Cu-g-C_3N_4, respectively.

Ion exchange reaction has been widely used in tuning the composition of ionic nanocrystals driven by the solubility difference of ions, thus allowing for the adjustment of optical properties and electric structure of obtained products [44–46]. In our earlier work, we found that protons could partially replace Na ions in layer-structured NaInS$_2$, while has no effect on transition metals in M-In-S (M = Zn, Mn, Cu etc.) ternary sulfides [43]. In this work, multi-metal doped g-C_3N_4 exhibited similar properties with ternary sulfide. In fact, g-C_3N_4 is prone to capture the metal ions due to different electric charge of cations and nitrogen atoms, and then form strong ion–dipole interaction ascribed to long pairs of electrons in the large cave between the connected thiazine structures of g-C_3N_4 [23]. Because of the variable ionic radii, valence states and electron configurations of metal ions, their interactions with nitrogen anions are quite different, and alkali metal ions possessed weaker binding capacity to nitrogen than that of transition metal ions. During protonation process, H$^+$ ions preferentially occupy the position of alkali metal ions due to the high reaction activity of doping sites original from structural distortion of g-C_3N_4, thus leads to the formation of protoned Cu-g-C_3N_4 (as shown in Eq. (1)). Compared to ionic nanocrystals, the building block of tri-s-triazine units may serve as anion framework and preserve well in the cations exchange reaction, which facilitates the maintenance of morphology compared to the broken texture of protonation of pristine g-C_3N_4 [34]. Another evidence is Mn doped g-C_3N_4, although protonation post-treatment had no effect on the existence of Mn, the change of the morphology could be well explained by the structural distortion of tri-s-triazine units in g-C_3N_4 by introduced protons [27]. It should be noted that the amount of Cu in g-C_3N_4 would decreased when treated with prolonged protonation time or higher concentrated acid. When protonated Cu-g-C_3N_4 is heated at high temperature, the deprotonation process (Eq. (2)) occurs and results in the formation of Cu doped g-C_3N_4 naontubes. The possibility for protonation and reversible process could ascribe to the potential base functionality (-C-N-) of nitrogen in g-C_3N_4 structure[34], which shows chemical properties similar to alkaline materials such as ammonia to some extent.

$$Cu-C_3N_4-M(M = K, Na, Li)Cl + HCl \rightarrow C_3N_4-(Cu, H)Cl + MCl$$
$$(1)$$

$$C_3N_4-(Cu, H)Cl(\xrightarrow{\Delta})Cu-C_3N_4 + HCl\uparrow$$
$$(2)$$

The photocatalytic activity of the obtained products was investigated by visible-light-induced hydrogen evolution from water splitting (Fig. 5). It is clear that bulk g-C_3N_4 prepared by directly polycondensation of melamine presented a low H$_2$ generation rate of 0.237 mmol h^{-1} g^{-1}. Increased H$_2$ evolution rates were obtained as 0.59 mmol h^{-1} g^{-1} for bulk Cu-g-C_3N_4 and 1.87 mmol h^{-1} g^{-1} for porous g-C_3N_4 nanotubes, as shown in Fig. 5a. Very encouragingly,

drastically improved photocatalytic H$_2$ generation as high as 3.02 mmol h^{-1} g^{-1} was found for Cu-g-C_3N_4 nanotubes, and this value is about 13 times higher than that of the bulk g-C_3N_4. In addition, comparisons of photocatalytic H$_2$ revolution over g-C_3N_4 based photocatalysts with different elemental doping were also presented in Table S1 of supporting information, demonstrating the superior photocatalytic property of as synthesized products. Furthermore, the photocatalytic activity of g-C_3N_4 nanotubes with different Cu doping amount were also investigated, and 0.05 wt. % Cu doped sample exhibited the highest photocatalytic activity for water splitting as shown in Fig. 5b. In addition, the influence of calcining temperature on the photocatalytic activity of obtained products was also investigated (Fig. S3). The crystallinity of synthesized products was monotonically increased with elevated temperature, while the photocatalytic H$_2$ generation rates were firstly increased and then sharply decreased. The highest photocatalytic activity was obtained with the product calcined at 550 °C.

It is of interest to explore the underlying reasons for enhanced photocatalytic activity of obtained products compared to pure g-C_3N_4. First, bulk Cu-g-C_3N_4 shows slightly increased specific surface area from 10.45 m^2 g^{-1} to 15.53 m^2 g^{-1} compared to pure bulk g-C_3N_4, and the enlarged visible light absorption is responsible for the improved photocatalytic property. While the mesoporous g-C_3N_4 nanotubes have a much higher surface area of 123 m^2 g^{-1} which may be accounted for the enhanced hydrogen evolution rate due to the abundant surface reaction sites offered by the higher specific surface area and widened light absorbance spectrum (Fig. 3d).

The kinetic properties of photoinduced carriers of different samples were further investigated (Fig. 6). Firstly, steady-state photoluminescence (PL) upon excitation at 397 nm was conducted to study the charge recombination under light excitation as shown in Fig. 6a. It could be observed that the intensity of emission peaks was progressively decreased from bulk g-C_3N_4, bulk Cu-g-C_3N_4, g-C_3N_4 nanotubes to Cu-g-C_3N_4 nanotubes, demonstrating the gradually enhanced separate efficiency of created charges. The lifetimes of modified C_3N_4 were further analyzed by the time-resolved fluorescence spectra (Fig. 6b). The average fluorescence lifetime increased from 2.61, 4.13 to 4.79 ns for bulk Cu-g-C_3N_4, g-C_3N_4 nanotubes and Cu-g-C_3N_4 nanotubes, respectively. Cu doped g-C_3N_4 nanotubes also exhibited the longest carrier lifetimes in all modified samples, indicating the highest charge separation and transfer efficiency, thereby positively preferred the photocatalytic hydrogen evolution.

Transient photocurrent response under visible light irradiation was conducted to further evaluate the charge transport property of as synthesized products, as shown in Fig. 6c. Cu-g-C_3N_4 nanotubes revealed the highest photocurrent density when compared with other samples, consistent with the H$_2$ evolution rates in Fig. 5a. This confirms the effective separation of photoinduced carriers during photocatalysis process. Fig. 6d displays the EIS spectra of synthesized photocayalysts. A significant decrease in semicircular Nyquist plots could be observed for
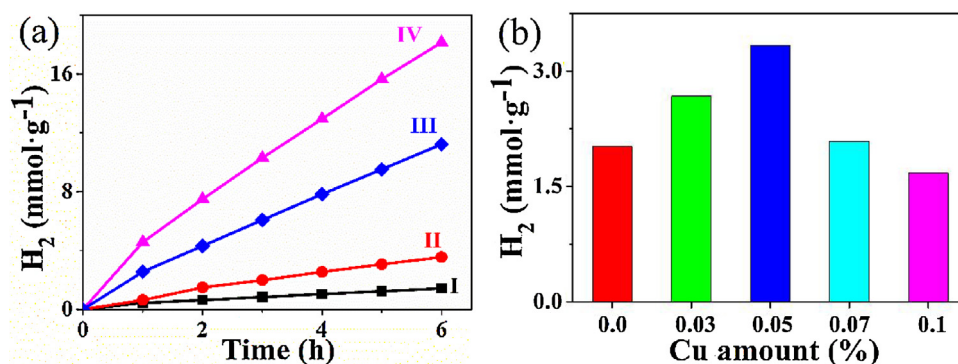

Fig. 5. (a) Photocatalytic H$_2$ generation rates of different samples. The curves I, II, III and IV curves in (a) represent the bulk g-C_3N_4, bulk Cu-g-C_3N_4, g-C_3N_4 nanotubes and Cu-g-C_3N_4 nanotubes, respectively. (b) photocatalytic H$_2$ generation rates of porous g-C_3N_4 nanotubes with different Cu doping amount.
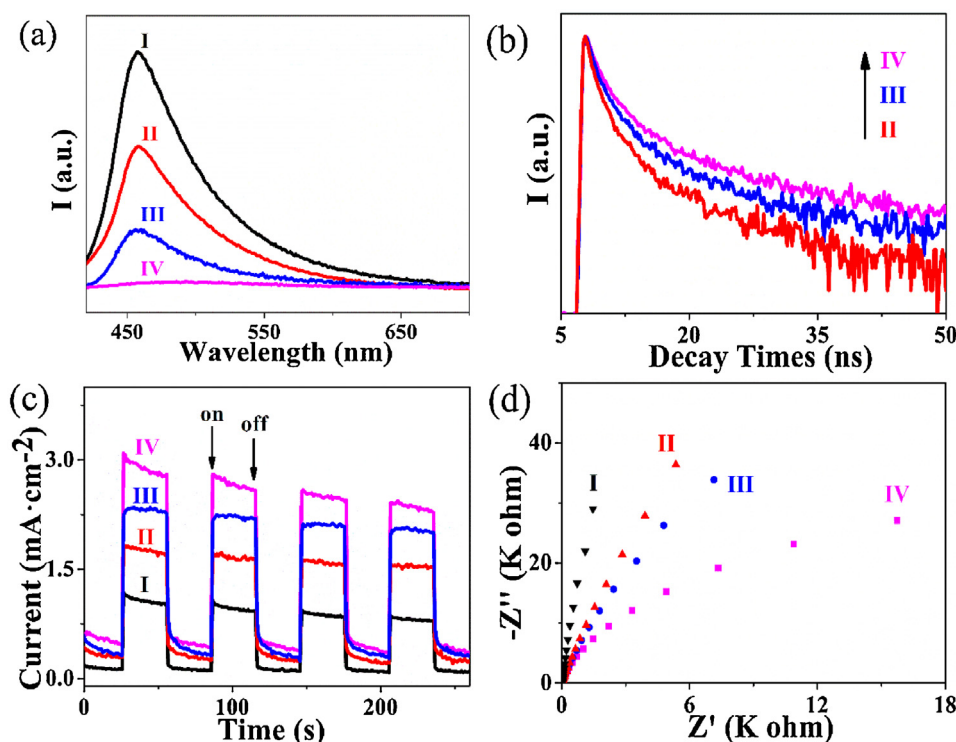
Fig. 6. (a) Steady-state PL spectra, (b) time-resolved PL spectra, (c) transient photocurrents and (d) EIS spectra of different samples. The curves I, II, III and IV in (a)–(d) represent the bulk g-C$_3$N$_4$, bulk Cu-g-C$_3$N$_4$, g-C$_3$N$_4$ nanotubes and Cu-g-C$_3$N$_4$ nanotubes, respectively.
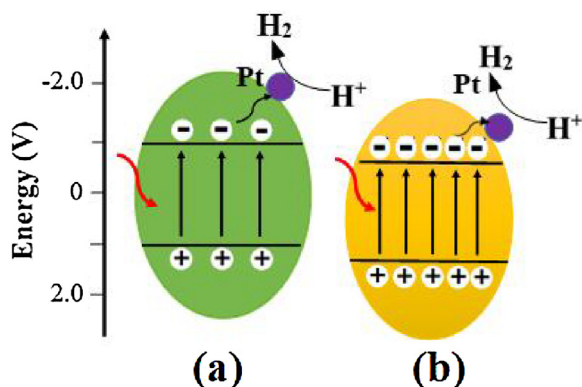

Fig. 7. Schematic illustration of the photocatalytic mechanism for (a) g-C$_3$N$_4$ and (b) Cu doped g-C$_3$N$_4$ nanotubes.

modified samples, suggesting suppressed resistance of working electrodes. Apparently, photocatalysts obtained by our proposed strategy exhibited the smallest arc radius, which is the most eff ;ective approach to improve the electronic conductivity and promote charge separation. These results well demonstrated the internal mechanism for enhanced photocatalytic activity of obtained products.

Based on above analysis, it is reasonable to summarize the increased photocatalytic properties for as-obtained Cu-g-C$_3$N$_4$ mesoporous nanotubes. When irradiated with visible light, photoexcited electrons can be excited to the conduction band of g-C$_3$N$_4$, then react with H$^+$ with the assisted of co-catalyst Pt to generate hydrogen gas. Due to the fast carrier recombination rate and low specific surface area of pristine bulk g-C$_3$N$_4$, limited electrons could transport to the active site and involved in the redox reactions, as a result low hydrogen was obtained. While for Cu-g-C$_3$N$_4$ mesoporous nanotubes, thanks to the increased light absorption and enhanced charge transfer and separation ability, much more photoexcited electrons could participate in the redox reactions Mesoporous nanostructure also provides shorter charge carrier

diffusion length, more channels and large surface active sites for mass transfer and redox reactions, resulting in a significant improvement of photocatalytic hydrogen evolution compared to pristine g-C$_3$N$_4$. A schematic illustration of the photocatalytic mechanism was shown in Fig. 7.

4. Conclusion

In this work, we have developed a new simple ion replacement process to synthesize mesoporous copper doped g-C$_3$N$_4$ nanotubes which were driven by the ion–dipole interaction of metal cations in g-C$_3$N$_4$. The tri-s-triazine units may serve as the stable framework in the ion exchange reaction. The porous microstructure, together with the improved visible light absorbance and well suppressed recombination of carriers, greatly enhanced the photocatalytic hydrogen evolution of obtained products, highlighting the advantage of our new synthetic strategy for designing efficient photocatalysts. The findings reported herein may lead to new opportunities for developing more efficient photocatalysts for potential applications in solar energy conversion.

Appendix A. Supplementary data

Supplementary material related to this article can be found, in the online version, at doi:https://doi.org/10.1016/j.apcatb.2018.04.020.

References

[1] X. Chen, L. Liu, P.Y. Yu, S.S. Mao, Science 331 (2011) 746–750.
[2] T.W. Kim, K.-S. Choi, Science 343 (2014) 990–994.

[3] K. Maeda, T. Takata, M. Hara, N. Saito, Y. Inoue, H. Kobayashi, K. Domen, J. Am. Chem. Soc. 127 (2005) 8286–8287.

[4] Z. Zhang, Y. Huang, K. Liu, L. Guo, Q. Yuan, B. Dong, Adv. Mater. 27 (2015) 5906–5914.

[5] P. Hu, S.S. Pramana, S. Cao, C.K. Ngaw, J. Lin, S.C.J. Loo, T.T.Y. Tan, Adv. Mater. 25 (2013) 2567–2572.

[6] Y. Shi, B. Zhang, Chem. Soc. Rev. 45 (2016) 1529–1541.

[7] Y.P. Yuan, L.W. Ruan, J. Barber, S.C. Joachim Loo, C. Xue, Energy Environ. Sci. 7 (2014) 3934–3951.

[8] M.G. Kibria, F.A. Chowdhury, S. Zhao, B. AlOtaibi, M.L. Trudeau, H. Guo, Z. Mi, Nat. Commun. 6 (2015) 6797–6798.

[9] Y. Zheng, J. Liu, J. Liang, M. Jaroniec, S.Z. Qiao, Energy Environ. Sci. 5 (2012) 6717–6731.

[10] X. Wang, K. Maeda, A. Thomas, K. Takanabe, G. Xin, J.M. Carlsson, K. Domen, M. Antonietti, Nat. Mater. 8 (2008) 76–80.

[11] S. Cao, J. Low, J. Yu, M. Jaroniec, Adv. Mater. 27 (2015) 2150–2176.

[12] W.J. Ong, L.L. Tan, Y.H. Ng, S.T. Yong, S.P. Chai, Chem. Rev. 116 (2016) 7159–7329.

[13] D. Masih, Y. Ma, S. Rohani, Appl. Catal. B Environ. 206 (2017) 556–588.

[14] Q. Han, B. Wang, Y. Zhao, C. Hu, L. Qu, Angew. Chem. Int. Ed. 54 (2015) 11433–11437.

[15] J. Zhang, F. Guo, X. Wang, Adv. Funct. Mater. 23 (2013) 3008–3014.

[16] D. Zheng, X.N. Cao, X. Wang, Angew. Chem. Int. Ed. 55 (2016) 11512–11516.

[17] M. Zhu, S. Kim, L. Mao, M. Fujitsuka, J. Zhang, X. Wang, T. Majima, J. Am. Chem. Soc. 139 (2017) 13234–13242.

[18] S.Z. Hu, X.Y. Qu, J. Bai, P. Li, Q. Li, L.J. Song, ACS Sustain. Chem. Eng. 5 (2017) 6863–6872.

[19] G. Zhang, M. Zhang, X. Ye, X. Qiu, S. Lin, X. Wang, Adv. Mater. 26 (2014) 805–809.

[20] M. Zhang, X. Wang, Energy Environ. Sci. 7 (2014) 1902–1906.

[21] J. Zhang, X. Chen, K. Takanabe, K. Maeda, K. Domen, J.D. Epping, X. Fu, M. Antonietti, X. Wang, Angew. Chem. Int. Ed. 49 (2010) 441–444.

[22] J. Wen, J. Xie, X. Chen, X. Li, Appl. Surf. Sci. 391 (2017) 72–123.

[23] L. Jiang, X. Yuan, Y. Pan, J. Liang, G. Zeng, Z. Wu, H. Wang, Appl. Catal. B Environ. 217 (2017) 388–406.

[24] T. Xiong, W. Cen, Y. Zhang, F. Dong, ACS Catal. 6 (2016) 2462–2472.

[25] S. Hu, F. Li, Z. Fan, F. Wang, Y. Zhao, Z. Lv, Dalton Trans. 44 (2015) 1084–1092.

[26] X. Wang, X. Chen, A. Thomas, X. Fu, M. Antonietti, Adv. Mater. 21 (2009) 1609–1612.

[27] L. Muniandy, F. Adam, A.R. Mohamed, A. Lqbal, N.R.A. Rahman, Appl. Surf. Sci. (398) (2017) 43–55.

[28] Z. Li, C. Kong, G. Lu, J. Phys. Chem. C 120 (2016) 56–63.

[29] S. Guo, Z. Deng, M. Li, B. Jiang, C. Tian, Q. Pan, H. Fu, Angew. Chem. Int. Ed. 55 (2016) 1830–1834.

[30] Z.A. Lan, G. Zhang, X. Wang, Appl. Catal. B Environ. 192 (2016) 116–125.

[31] J. Sun, J. Zhang, M. Zhang, M. Antonietti, X. Fu, X. Wang, Nat. Commun. 3 (2012) 1139-7.

[32] S. Gupta, S.V. Kershaw, A.L. Rogach, Adv. Mater. 25 (2013) 6923–6944.

[33] H. Gao, S. Yan, J. Wang, Y.A. Huang, P. Wang, Z. Li, Z. Zou, Phys. Chem. Chem. Phys. 15 (2013) 18077–18084.

[34] Y. Zhang, A. Thomas, M. Antonietti, X. Wang, J. Am. Chem. Soc. 131 (2009) 50–51.

[35] A. Thomas, A. Fischer, F. Goettmann, M. Antonietti, J.-O. Muller, R. Schlogl, J.M. Carlsson, J. Mater. Chem. 18 (2008) 4893–4908.

[36] Z. Ding, X. Chen, M. Antonietti, X. Wang, ChemSusChem 4 (2011) 274–281.

[37] J. Zhang, M. Zhang, C. Yang, X. Wang, Adv. Mater. 26 (2014) 4121–4126.

[38] Y.P. Yuan, L.S. Yin, S.W. Cao, L.N. Gu, G.S. Xu, P. Du, H. Chai, Y.-S. Liao, C. Xue, Green Chem. 16 (2014) 4663–4668.

[39] Y. Guo, J. Li, Y. Yuan, L. Li, M. Zhang, C. Zhou, Z. Lin, Angew. Chem. Int. Ed. 55 (2016) 14693–14697.

[40] H. Gao, S. Yan, J. Wang, Z. Zou, Dalton Trans. 43 (2014) 8178–8183.

[41] G.H. Dong, K. Zhao, L.Z. Zhang, Chem. Commun. 48 (2012) 6178–6180.

[42] T. Xiong, Wl. Cen, Y.X. Zhang, F. Dong, ACS Catal. (6) (2016) 2462–2472.

[43] P. Hu, C.K. Ngaw, Y. Yuan, P.S. Bassi, S.C. Joachim Loo, T.T. Yang Tan, Nano Energy 26 (2016) 577–585.

[44] P. Hu, C.K. Ngaw, Y.Y. Tay, S. Cao, J. Barber, T.T.Y. Tan, S.C.J. Loo, Chem. Commun. 51 (2015) 9381–9384.

[45] D.H. Son, S.M. Hughes, Y. Yin, A. Paul Alivisatos, Science 306 (2004) 1009.

[46] X. Wu, Y. Yu, Y. Liu, Y. Xu, C. Liu, B. Zhang, Angew. Chem. Int. Ed. 51 (2012) 3211–3215.